Polytetrafluoroethylene mediated contact-electro-catalysis enhanced permanganate activation: unraveled mechanism involving singlet oxygen and manganese species

Yang Liu [1, 2, 4], Hao Duo [4], Takeshi Kawaguchi [4], Hiroaki Sakamoto (🖂)[4], Jie Wang (🖂)[1, 2, 3, 5]

1 State Key Laboratory of Advanced Separation Membrane Materials, Tiangong University, Tianjin 300387, China

2 School of Material Science and Engineering, Tiangong University, Tianjin 300387, China

3 School of Environmental Science and Engineering, Tiangong University, Tianjin 300387, China

4 Graduate School of Engineering, University of Fukui, Fukui 910-8507, Japan

5 Hebei Industrial Technology Research Institute of Membranes, Cangzhou Institute of Tiangong University, Cangzhou 061000, China

The SI included: **5 Texts, 3 Tables, 14 Figures.**

🖂 Corresponding authors

E-mail: wangjie@tiangong.edu.cn (J. Wang); hi-saka@u-fukui.ac.jp (H. Sakamoto)

Lists of Captions:

Text S1. Stock solution preparation and experimental procedure

Text S2. Electrochemical measurement

Text S3. The degradation of pollutants in the process followed pseudo-first-order kinetics

Text S4. Energy consumption and conversion efficiency

Text S5. Density functional theory calculation

Table S1 HPLC parameters for selected compounds

Table S2 Comparison of different activation methods for CEC

Table S3 Comparative of dye and pollutant degradation using CEC systems and Mn(VII)-based activation technologies

Fig. S1 Experiment setup photograph for catalytic degradation. Ultrasound bath working conditions: 45 kHz, 100 W.

Fig. S2 (a) and (b) Mn(VII) degradation of different dosages of RHB and MB, (c) and (d) RHB and MB removal by different dosages of PTFE. Experimental conditions: $[Mn(VII)]_0$ = 0.06 mmol/L, pH = 7.0, and ultrasonic frequency = 45 kHz, T= 25℃ ± 2℃.

Fig. S3 The conceptual model for interfacial reaction sites affected by dosage of PTFE. (a) less dosage, (b) optimal dosage, and (c) excessive dosage of PTFE.

Fig. S4 (a) and (b) show the voltage output and current output under different systems, respectively. Experimental conditions: $[Mn(VII)]_0$ = 0.06 mmol/L, $[PTFE]_0$

= 400 mg/L, pH = 7.0, ultrasonic frequency = 45 kHz, temperature = 25℃ ± 2℃.

Fig. S5 DFT calculations of the LUMO and HOMO levels for H_2O-PTFE, and PTFE-Mn(VII) without ultrasound (normal pressure) and with ultrasound (high pressure).

Fig. S6 Fluorescence spectral changes during (a) US-PTFE and (b) Mn(VII) in aqueous coumarin solution. Experimental conditions: $[\text{Mn(VII)}]_0$ = 0.20 mmol/L, $[\text{PTFE}]_0$ = 400 mg/L, $[\text{coumarin}]_0 = 1 \times 10^{-3}$ mol/L, pH = 7.0, EX = 335 nm.

Fig. S7 Amount of Mn(III) in the US-PTFE-Mn(VII) system in the presence of different concentrations of pyrophosphate (PP). The PP concentrations in (a), (b), (c), and (d) are 0 mmol/L, 0.5 mmol/L, 2.5 mmol/L, and 5.0 mmol/L, respectively. Experimental conditions: $[\text{Mn(VII)}]_0$ = 0.03 mmol/L, $[\text{PTFE}]_0$ = 400 mg/L, pH = 7.0, ultrasonic frequency = 45 kHz, T = 25℃ ± 2℃.

Fig. S8 Amount of Mn(III) in the US-PTFE-Mn(VII) system in the presence of different concentrations of pyrophosphate (PP). The PP concentrations in (a), (b), (c), and (d) are 0 mmol/L, 0.5 mmol/L, 2.5 mmol/L, and 5.0 mmol/L, respectively. Experimental conditions: $[\text{Mn(VII)}]_0$ = 0.06 mmol/L, $[\text{PTFE}]_0$ = 400 mg/L, pH = 7.0, ultrasonic frequency = 45 kHz, T = 25℃ ± 2℃.

Fig. S9 Amount of Mn(III) in the US-PTFE-Mn(VII) system in the presence of different concentrations of pyrophosphate (PP). The PP concentrations in (a), (b), (c), and (d) are 0 mmol/L, 0.5 mmol/L, 2.5 mmol/L, and 5.0 mmol/L, respectively. Experimental conditions: $[\text{Mn(VII)}]_0$ = 0.20 mmol/L, $[\text{PTFE}]_0$ = 400 mg/L, pH = 7.0, ultrasonic frequency = 45 kHz, T = 25℃ ± 2℃.

Fig. S10 (a) PMSO content and corresponding $PMSO_2$ yield in the Mn(VII) alone system, and (b) PMSO content and corresponding $PMSO_2$ yield in the US-PTFE-Mn(VII) system. Experimental conditions: $[Mn(VII)]_0$ = 0.15 mmol/L, $[PMSO]_0$ = 100 μmol/L, $[PTFE]_0$ = 400 mg/L, pH = 7.0, and ultrasonic frequency = 45 kHz, T= 25℃ ± 2℃.

Fig. S11 The effect of adding PMSO on the removal efficiency of RHB (a) and MB (a) in different systems. Experimental conditions: $[RHB]_0$ = $[MB]_0$ = 10 mg/L, $[Mn(VII)]_0$ = 0.06 mmol/L, $[PMSO]_0$ = 100.0 μmol/L, $[PTFE]_0$ = 400 mg/L, pH = 7.0, and ultrasonic frequency = 45 kHz, T= 25℃ ± 2℃.

Fig. S12 Characteristic peaks of MnO_2 in the US-PTFE-Mn(VII) system. Experimental conditions: $[Mn(VII)]_0$ = 0.06 mmol/L, $[PTFE]_0$ = 400 mg/L, pH = 7.0, and ultrasonic frequency = 45 kHz, T= 25℃ ± 2℃.

Fig. S13 Degradation results of RHB (a) and MB (b) by MnO_2 in the US-PTFE-Mn(VII) system. Experimental conditions: $[RHB]_0$ = $[MB]_0$ = 10 mg/L, $[Mn(VII)]_0$ = 0.06 mmol/L, $[PTFE]_0$ = 400 mg/L, pH = 7.0, T= 25℃ ± 2℃.

Fig. S14 Comparison of removal efficiency and energy consumption for different activated CEC methods in dye degradation.

SI Texts

Text S1. Stock solution preparation and experimental procedure

The stock dye solution of RHB and MB (250 mg/L) was first prepared. For each experiment, 0.2 mL of this solution was diluted in 50 mL of water, resulting in a final dye concentration of 10 mg/L. A 7.5 mmol/L (1.185 g/L) Mn(VII) solution was freshly prepared by dissolving 0.1185 g of Mn(VII) in 100 mL of water. Subsequently, 0.4 mL of this solution was added to 50 mL of the dye-containing solution, achieving a final Mn(VII) concentration of 0.06 mmol/L. The reaction was terminated by the addition of 20 μL of hydroxylamine hydrochloride (0.1 mol/L) at the end of the experiment.

Radical quenching and scavenging experiments were conducted as follows: 0.2 mL of methanol (for •OH) was added dropwise to 50 mL of the solution, resulting in a final methanol concentration of 0.1 mol/L. Similarly, 0.478 mL of tert-butanol (for •OH) was added to 50 mL of the solution, yielding a tert-butanol concentration of 0.1 mol/L. To prepare a 0.1 mol/L solution of p-benzoquinone (for $O_2^{\bullet-}$), 0.5 g was dissolved in 50 mL of water. For silver nitrate ($AgNO_3$) (for electron transfer), 4.247 g was dissolved in 10 mL of water, and 0.2 mL of this stock solution was added to 50 mL of water, resulting in a final $AgNO_3$ concentration of 0.01 mol/L. L-Histidine (L-His) (for $^1O_2$) was dissolved by dissolving 0.7758 g in 50 mL of water, yielding a concentration of 0.1 mol/L. Sodium azide (NaN_3) (for $^1O_2$) was dissolved by dissolving 1.625 g in 10 mL of water, and 0.2 mL of this solution was added to 50 mL of water, resulting in a final concentration of 0.01 mol/L. To prepare a 0.1 g/L solution of Catalase (for H_2O_2), 5 mg was directly dissolved in 50 mL of water. The radical traps, DMPO, and TEMP were prepared with concentrations of 100 mmol/L and 50 mmol/L, respectively.

Mn(III)-PP: The 0.25 mol/L pyrophosphate (PP) solution was prepared by dissolving 1.1151 g in 10 mL of water, with the pH adjusted to 7.0. Aliquots of 0.02 mL, 0.2 mL, and 1 mL of this solution were added to 50 mL of water, yielding final concentrations of 0.1 mmol/L, 1 mmol/L, and 5 mmol/L, respectively.

Mn(VI)/Mn(V)：Because PMSO can be oxidized by high-valent metal-oxo species (such as Mn = O and Fe = O) via an oxygen atom transfer process (OAT) to produce the corresponding sulfone compound (i.e., methyl phenyl sulfone, $PMSO_2$). On one hand, the generation rate of intermediate RMnS in the system can be evaluated by observing the changes in the PMSO degradation rate and the formation rate of $PMSO_2$ in different systems. On the other hand, by comparing the dye degradation efficiency under varying PMSO concentrations (0.05 mmol/L, 0.10 mmol/L, and 0.20 mmol/L), the roles of Mn(VI)/Mn(V) in the system can be assessed.

Mn(V): Mn(V) can be quenched by Ba^{2+} due to the formation of a precipitate between Ba^{2+} and Mn(V). By comparing different concentrations of Ba^{2+} (0.05 mmol/L, 0.10 mmol/L, and 0.20 mmol/L), the role of Mn(V) in dye degradation within the US-PTFE-Mn(VII) system can be determined.

Text S2. Electrochemical measurement

Electrochemical measurements were carried out in 50 mL of Mn(VII) solution (pH = 7.0) using a standard three-electrode configuration, with an Ag/AgCl electrode as the reference electrode, a platinum plate as the counter electrode, and a glassy carbon electrode as the working electrode.

Measured parameters of cyclic voltammetry (CV) curves: the voltage range was from −1.5 V to 1.5 V, with a scan rate of 0.1 V/s.

Text S3. The degradation of pollutants in the process followed pseudo-first-order kinetics

The degradation of pollutants in different systems followed pseudo-first-order kinetics, with good inverse correlation ($R^2 > 0.95$). The degradation rate can be calculated using the following equation:

$$\ln\left(\frac{[C]_t}{[C]_0}\right) = -K_{obs}t$$

Where $[C]_0$ and $[C]_t$ represent the concentrations of micropollutants at the initial time and at a defined time, respectively. K_{obs} is the pseudo-first-order rate constant (unit: $\min^{-1}$), and t is the reaction time.

Text S4. Energy consumption and conversion efficiency

The energy consumption of each treatment system was calculated using the following equations. The total energy consumption E_1 is given by:

$$\mathrm{E_1 = P \times T}$$

where P is the power of the equipment (kW) and T is the operating time (h). The energy consumption per milligram of pollutant removed, $E_{\text{per mg}}$, was then calculated as:

$$E_{\text{per mg}} = \frac{E_1 \times 3.6 \times 10^6}{m_{\text{removed}}}$$

where m_{removed} is the mass of the pollutant removed (mg), and the factor 3.6×10^6 converts kWh to joules. This method allows a direct comparison of the energy efficiency of different pretreatment or activation systems for pollutant degradation.

Text S5. Density functional theory calculation

Because the energy difference between the acceptor LUMO level and the donor HOMO level can be regarded as the electronic transfer energy (Wang et al., 2022), it can therefore be used to verify the possible electron-transfer pathways between PTFE and water/Mn(VII) molecules. All DFT calculations were carried out via Dmol3 module in Materials Studio 2019 (Ma et al., 2024). The generalized gradient approximation (GGA) with Perdew-Burke-Ernzerhof (PBE) functional was utilized to treat the exchange-correlation interaction (Wang et al., 2022). Owing to the weak-coupling limit, i.e., a negligeable overlap of the molecular orbital, the difference between the LUMO of the acceptor and the HOMO of the donor is considered as equivalent to the charge transfer energy (Lai et al., 2025). A double numerical quality basis set with d-type polarization function (DNP) was utilized for all the geometric optimizations, total energy calculations (Delley, 1990). The effective core pseudopotentials by Dolg and Bergner were used to model the core electrons (Dolg et al., 1987).

All the calculations were spin unrestricted. The conductor-like screening model (COSMO) with dielectric constant of 78.54 was used to simulate a solvent environment for the calculation. The effect of the Electric Double Layer has been neglected. The positions of all the atoms were fully relaxed until the following convergence criterion were met respectively: 0.002 Ha/Å for force, 10^{-5} Ha for total energy and 0.005 Å for displacement. The real space cutoff radius was 4.1 Å. The self-consistent field computations criterion was set at 10^{-6} Ha.

The transient collapse of cavitation bubbles could result in high pressure (around 100 MPa). The PTFE micro-particles are regarded to undergo elastic compression in the calculation since micro-particles of polymers can behave elastically beyond the linear region (Wang et al., 2022). he transient collapse of cavitation bubbles could result in high pressure (around 100 MPa). The compression of volume from 10 × 10 × 10 Å to 10 × 7 × 10 Å was regarded as equivalent to the high pressure environment induced by the collapse of cavitation bubbles.

SI Tables

Table S1 HPLC parameters for selected compounds

Compound	Mobile phase (v/v)	Wavelength (nm)
PMSO	acetonitrile/ acetic acid = 35/65	264
$PMSO_2$	acetonitrile/ acetic acid = 35/65	264

Table S2 Comparison of different activation methods for CEC

Methods	Power (kW)	Duration (h)	Efficiency (%)	References
Ball milling	2.0-3.0[a]	1-2	60-99.18	(Wang et al., 2024d)
Ultrasound	0.1-0.6[b]	3	25-99	(Dong et al., 2022; Zhao et al., 2023b)
Stirring	0.1-0.3[c]	6-56	60-99.60	(Ruan et al., 2022; Tang et al., 2022; Tang et al., 2023)

[a] The power data of the ball milling equipment comes from the planetary ball mill series of Fritsch GmbH (PULVERISETTE 5 premium line, Germany);

[b] The ultrasonic treatment was performed using an ultrasonic cleaner (Yumeng, JTS-1024, 40 kHz, 120 W);

[c] The stirring was performed using a magnetic stirrer (IKA C-MAG HS 7, 100 W, Germany) at 1000 r/min.

Table S3 Comparative of dye and pollutant degradation using CEC systems and Mn(VII)-based activation technologies

Frequency Energy / Stirring speed (r/min)	CEC system/ Activation system	Pollutant	Degradation efficiency	References
45 kHz, 110 W	PTFE-Mn(VII) (60 μmol/L)	RHB (C = 10mg/L; V = 100 mL) MB (C = 10mg/L; V = 100 mL)	RHB: 0.11771 min^{-1} MB: 0.1088 min^{-1}	**This study**
40 kHz, 600 W	FEP	MO (C = 5mg/L; V = 50 mL)	0.0364 min^{-1}	(Dong et al., 2022)
40 kHz, 500 W	PTFE	SMX: (C = 1mg/L; V = 50 mL) CIP: (C = 1mg/L; V = 50 mL) TET: (C = 1mg/L; V = 50 mL)	SMX: 0.0077 min^{-1} CIP：0.0179 min^{-1} TET：0.0256 min^{-1}	(Cao et al., 2024b)
1000 r/min	PTFE	MO (C = 5mg/L; V = 100 mL) RHB (C = 5mg/L; V = 100 mL) MB (C = 5mg/L; V = 100 mL)	MO：0.00325 h^{-1} RHB：0.1026 h^{-1} MB：0.0654 h^{-1}	(Wu et al., 2025)
500 r/min	PTFE	RHB (C = 5mg/L; V = 30 mL)	0.0056 h^{-1}	(Wu et al., 2022)
500 r/min	PTFE-$Bi_{12}TiO_{20}$	RHB (C = 5mg/L; V = 30 mL)	0.3721 h^{-1}	(Yingying et al., 2022)
40 kHz, 110 W	PTFE-PMS	SDZ (C = 10mg/L; V = 40 mL)	0.03003 min^{-1}	(Ma et al., 2024)
45 kHz 600 W	2D(CFx)n	MO (C = 5mg/L; V = 50 mL)	0.0185 min^{-1}	(Yin et al., 2024)
Poled BZT 2.5 kV/mm with 1200 r/min	BZT-PTFE	RHB (C = 5mg/L; V = 100 mL)	0.07698 h^{-1}	(Tang et al., 2022)
40 kHz, 120 W with 600 r/min	Fe_3O_4 @SiO_2 (R)	MO (C = 5mg/L; V = 50 mL)	0.0383 min^{-1}	(Chen et al., 2023)
40 kHz	RGO/ZnO	MG (C = 5mg/L; V = 50 mL)	0.03179 min^{-1}	(Yadav et al., 2024)
40 kHz, 840 W	CNTs-Mn(VII) (200 μmol/L)	CIP (C = 6.63 mg /L; V = 250 mL)	0.100 min^{-1}	(Wang et al., 2021)

300 r/min	Graphite-Mn(VII) (300 μmol/L)	SMX (C = 5.07 mg /L; V = 200 mL)	0.0989 min^{-1}	(Peng et al.)
VL (100 mW/cm^2)	g-C_3N_4- Mn(VII) (50 μmol/L)	SMX (C = 2.53 mg /L; V = 50 mL)	0.01046 min^{-1}	(Zhang et al., 2024)
UVA-LED (21.2 mW/cm^2)	UV- Mn(VII) (200 μmol/L)	DCF (C = 1.48 mg /L; V = 50 mL) 4-CP (C = 0.643 mg /L; V = 50 mL)	DCF: 0.05 min^{-1} 4-CP: 1.1 min^{-1}	(Yang et al., 2022)

The full names of the pollutant abbreviations：VL (Visible Light); MO (Methyl Orange)；RHB (Rhodamine B); MG (Malachite Green); PMS (potassium monopersulfate triplet salt); SDZ (Sulfadiazine); SMX (Sulfamethoxazole); CIP (Ciprofloxacin); TET (Tetracycline); CNTs (Commercial carbon nanotubes); BZT (Ba($Zr_{0.05}Ti_{0.95}$)O_3); DCF (diclofenac); 4-CP (4-chlorophenol).

SI Figures

Fig. S1 Experiment setup photograph for catalytic degradation. Ultrasound bath working conditions: 45 kHz, 100 W.

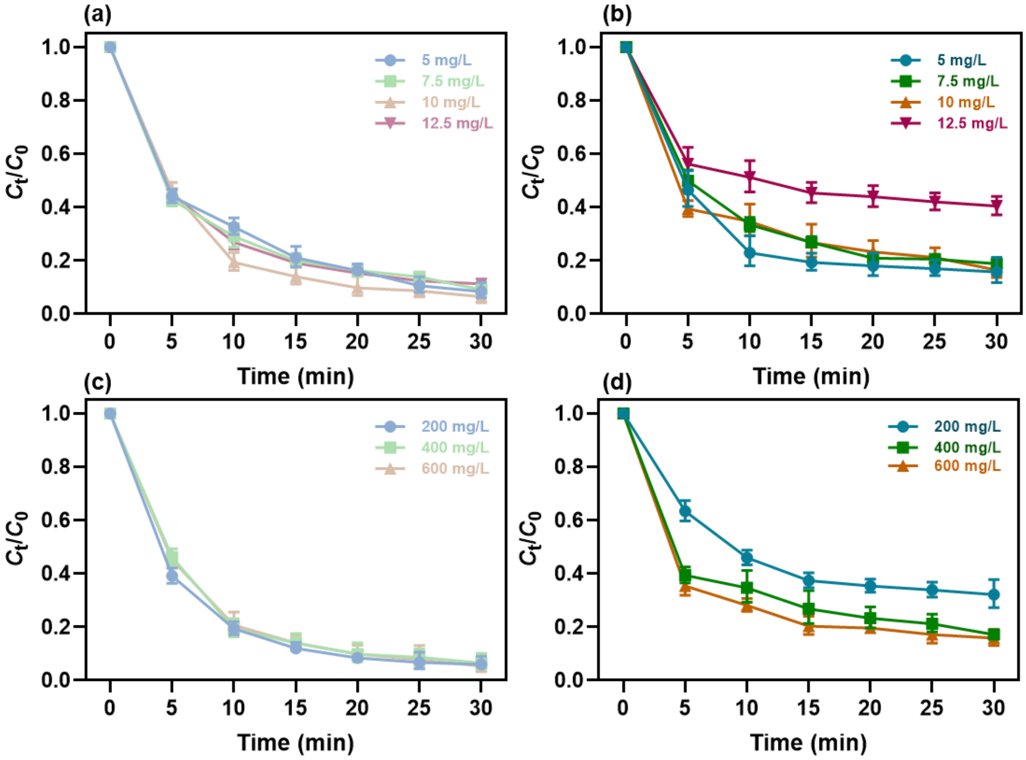

Fig. S2 (a) and (b) Mn(VII) degradation of different dosages of RHB and MB, (c) and (d) RHB and MB removal by different dosages of PTFE. Experimental conditions: $[Mn(VII)]_0$ = 0.06 mmol/L, pH = 7.0, and ultrasonic frequency = 45 kHz, T= 25℃ ± 2℃.

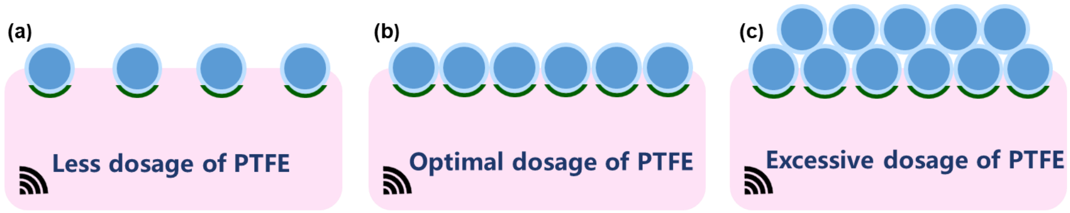

Fig. S3 The conceptual model for interfacial reaction sites affected by dosage of PTFE. (a) less dosage, (b) optimal dosage, and (c) excessive dosage of PTFE.

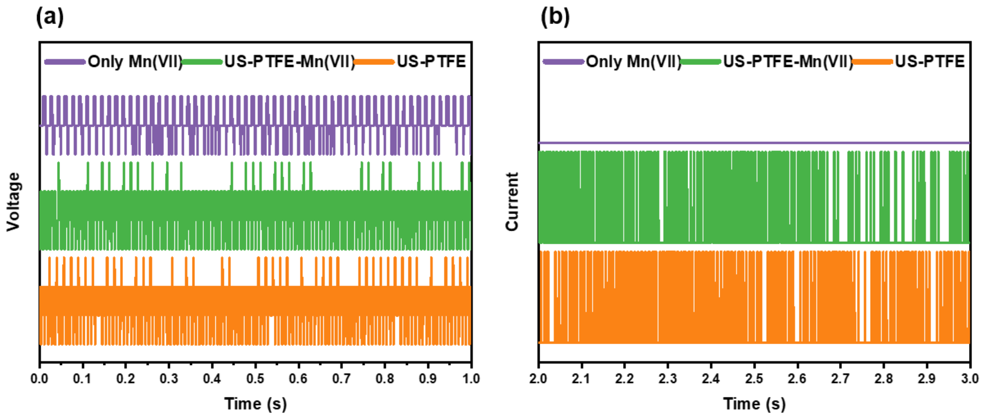

Fig. S4 (a) and (b) show the voltage output and current output under different systems, respectively. Experimental conditions: $[Mn(VII)]_0$ = 0.06 mmol/L, $[PTFE]_0$ = 400 mg/L, pH = 7.0, ultrasonic frequency = 45 kHz, temperature = 25℃ ± 2℃.

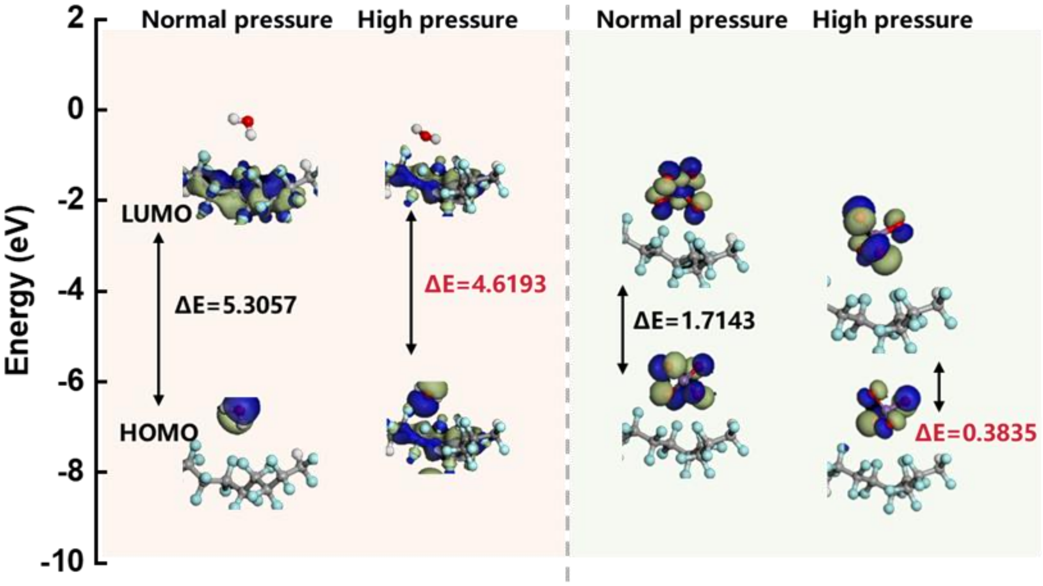

Fig. S5 DFT calculations of the LUMO and HOMO levels for H_2O-PTFE, and PTFE-Mn(VII) without ultrasound (normal pressure) and with ultrasound (high pressure).

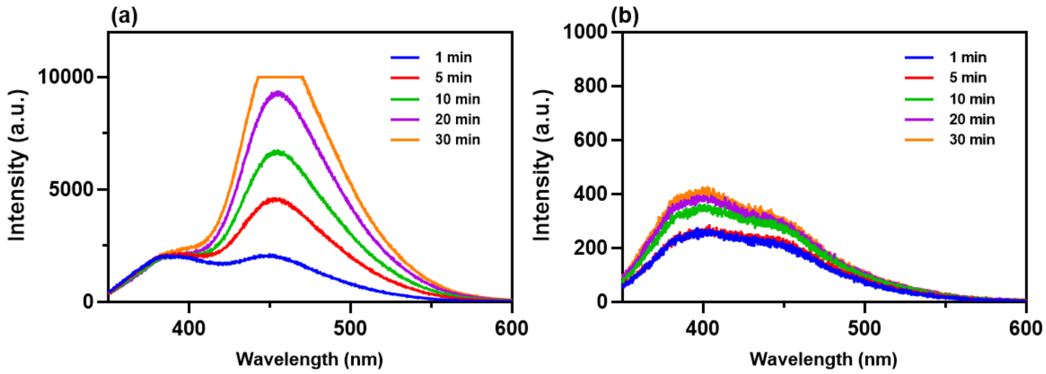

Fig. S6 Fluorescence spectral changes during (a) US-PTFE and (b) Mn(VII) in aqueous coumarin solution. Experimental conditions: $[\mathrm{Mn(VII)}]_0 = 0.20$ mmol/L, $[\mathrm{PTFE}]_0 = 400$ mg/L, $[\mathrm{coumarin}]_0 = 1 \times 10^{-3}$ mol/L, pH = 7.0, EX = 335 nm.

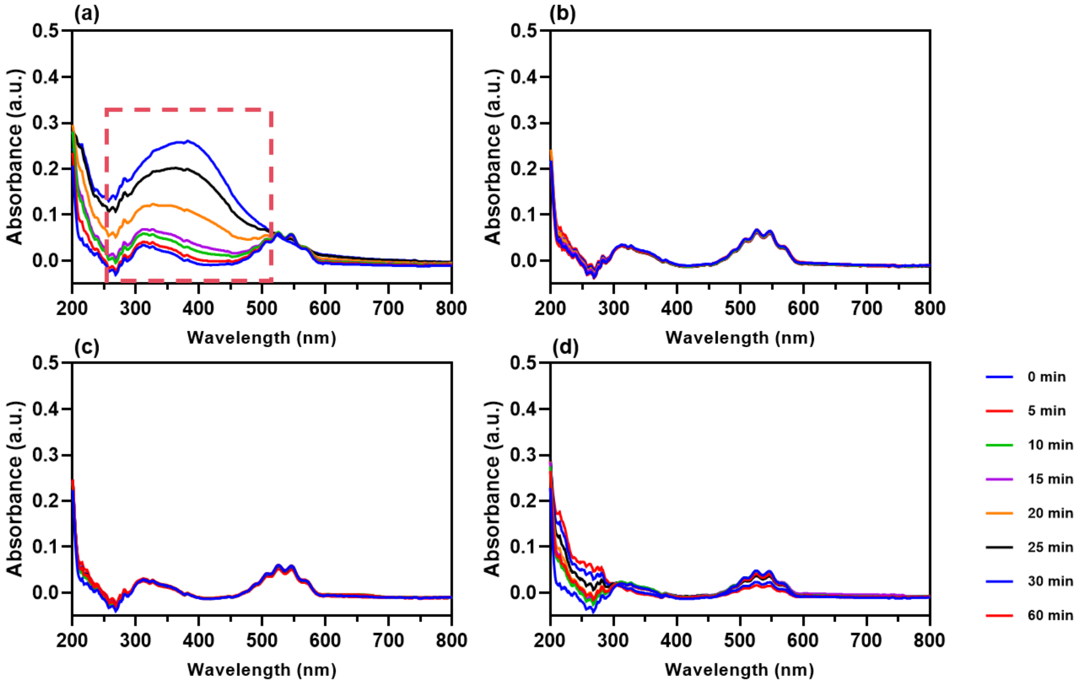

Fig. S7 Amount of Mn(III) in the US-PTFE-Mn(VII) system in the presence of different concentrations of pyrophosphate (PP). The PP concentrations in (a), (b), (c), and (d) are 0 mmol/L, 0.5 mmol/L, 2.5 mmol/L, and 5.0 mmol/L, respectively. Experimental conditions: $[Mn(VII)]_0 = 0.03$ mmol/L, $[PTFE]_0 = 400$ mg/L, pH = 7.0, ultrasonic frequency = 45 kHz, T = 25℃ ± 2℃.

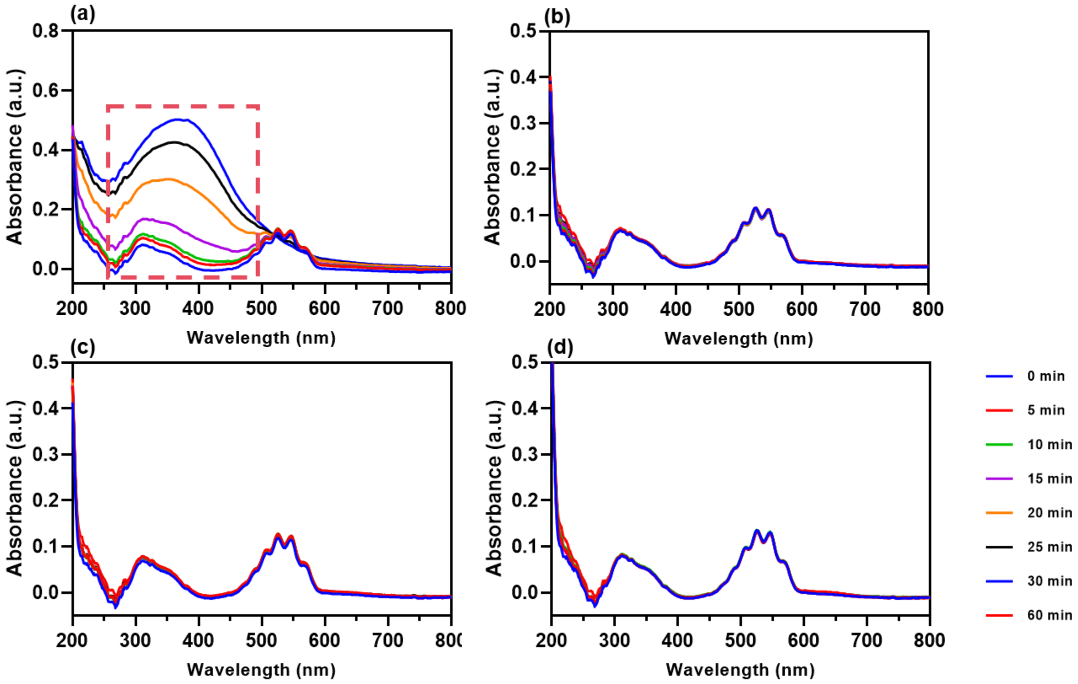

Fig. S8 Amount of Mn(III) in the US-PTFE-Mn(VII) system in the presence of different concentrations of pyrophosphate (PP). The PP concentrations in (a), (b), (c), and (d) are 0 mmol/L, 0.5 mmol/L, 2.5 mmol/L, and 5.0 mmol/L, respectively. Experimental conditions: $[Mn(VII)]_0$ = 0.06 mmol/L, $[PTFE]_0$ = 400 mg/L, pH = 7.0, ultrasonic frequency = 45 kHz, T = 25℃ ± 2℃.

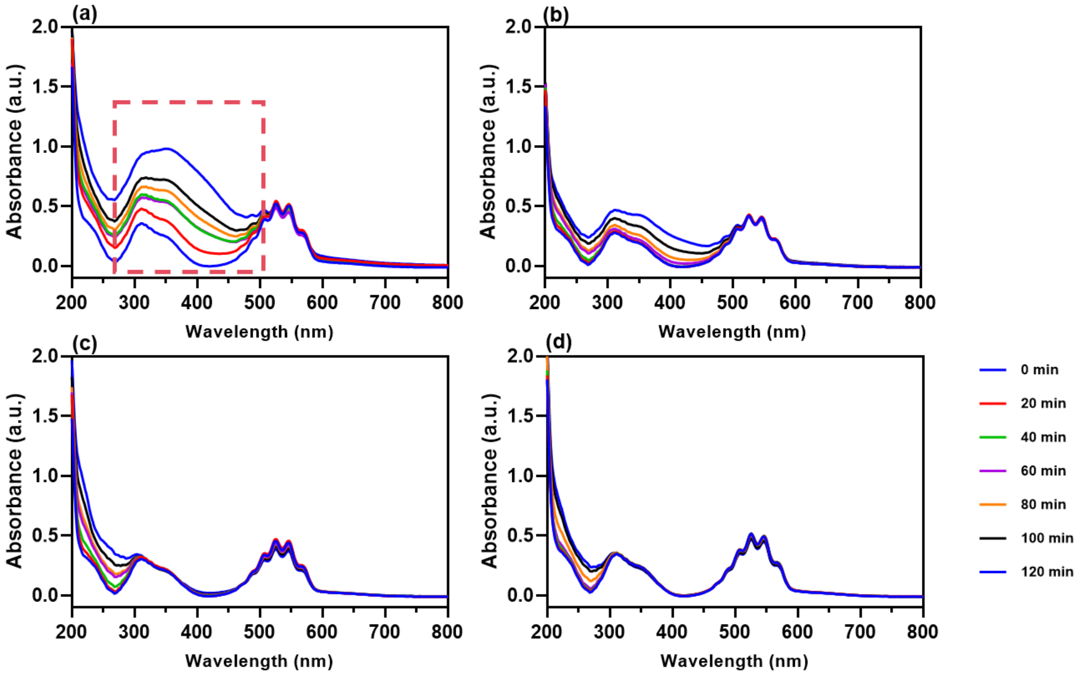

Fig. S9 Amount of Mn(III) in the US-PTFE-Mn(VII) system in the presence of different concentrations of pyrophosphate (PP). The PP concentrations in (a), (b), (c), and (d) are 0 mmol/L, 0.5 mmol/L, 2.5 mmol/L, and 5.0 mmol/L, respectively. Experimental conditions: $[\mathrm{Mn(VII)}]_0 = 0.20$ mmol/L, $[\mathrm{PTFE}]_0 = 400$ mg/L, pH = 7.0, ultrasonic frequency = 45 kHz, T = 25℃ ± 2℃.

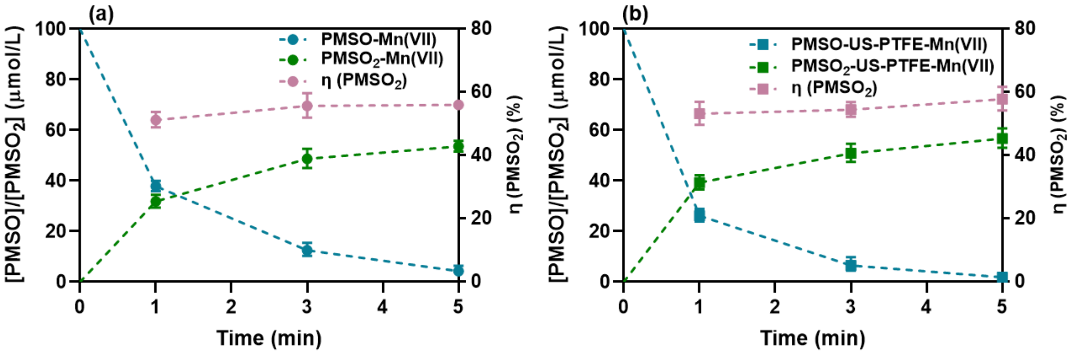

Fig. S10 (a) PMSO content and corresponding $PMSO_2$ yield in the Mn(VII) alone system, and (b) PMSO content and corresponding $PMSO_2$ yield in the US-PTFE-Mn(VII) system. Experimental conditions: $[Mn(VII)]_0$ = 0.15 mmol/L, $[PMSO]_0$ = 100 μmol/L, $[PTFE]_0$ = 400 mg/L, pH = 7.0, and ultrasonic frequency = 45 kHz, T= 25℃ ± 2℃.

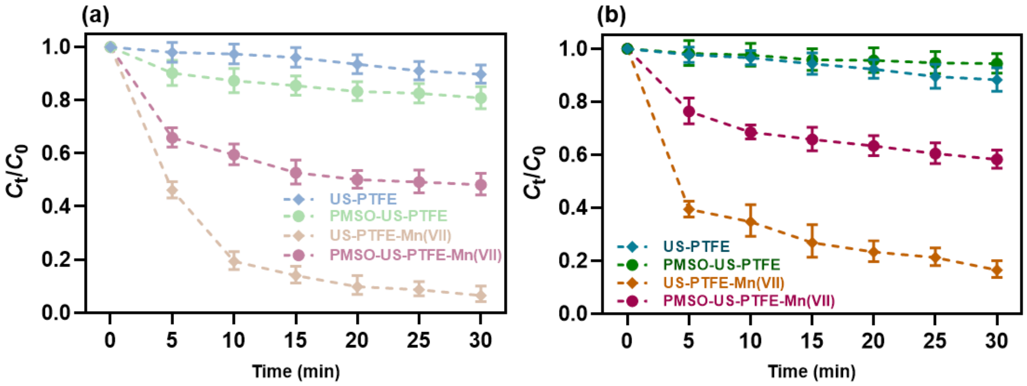

Fig. S11 The effect of adding PMSO on the removal efficiency of RHB (a) and MB (a) in different systems. Experimental conditions: $[RHB]_0 = [MB]_0 = 10$ mg/L, $[Mn(VII)]_0 = 0.06$ mmol/L, $[PMSO]_0 = 100.0$ μmol/L, $[PTFE]_0 = 400$ mg/L, pH = 7.0, and ultrasonic frequency = 45 kHz, T= 25℃ ± 2℃.

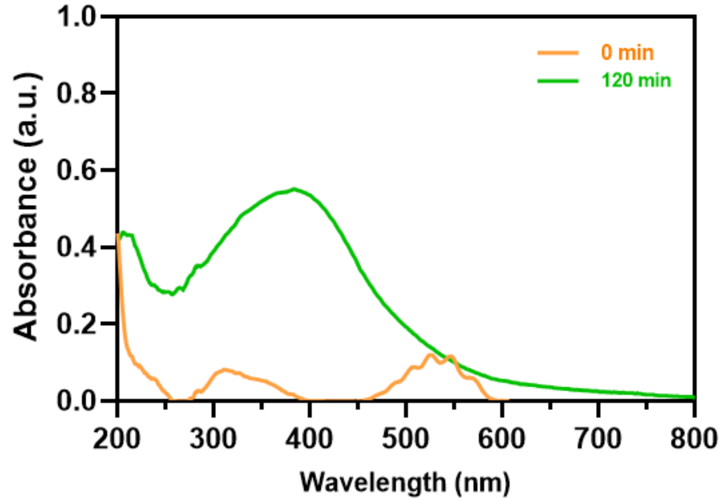

Fig. S12 Characteristic peaks of MnO_2 in the US-PTFE-Mn(VII) system.

Experimental conditions: $[Mn(VII)]_0 = 0.06$ mmol/L, $[PTFE]_0 = 400$ mg/L, pH = 7.0, and ultrasonic frequency = 45 kHz, T= 25℃ ± 2℃.

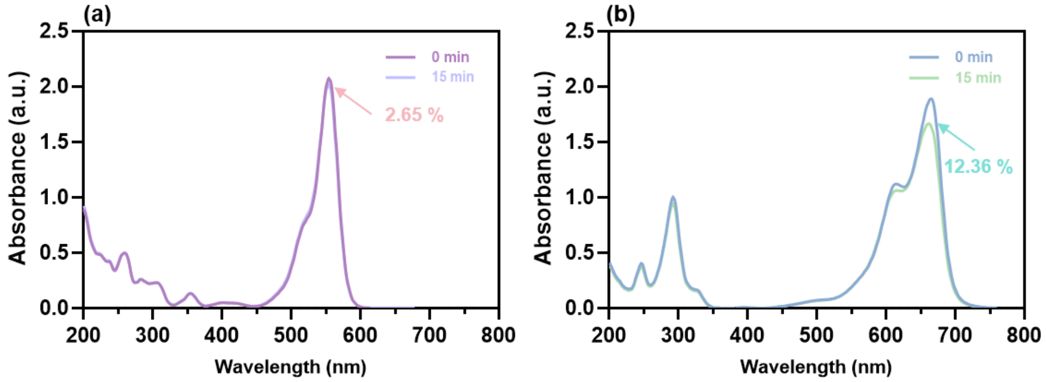

Fig. S13 Degradation results of RHB (a) and MB (b) by MnO_2 in the US-PTFE-Mn(VII) system. Experimental conditions: $[RHB]_0 = [MB]_0 = 10$ mg/L, $[Mn(VII)]_0 = 0.06$ mmol/L, $[PTFE]_0 = 400$ mg/L, pH = 7.0, T= 25℃ ± 2℃.

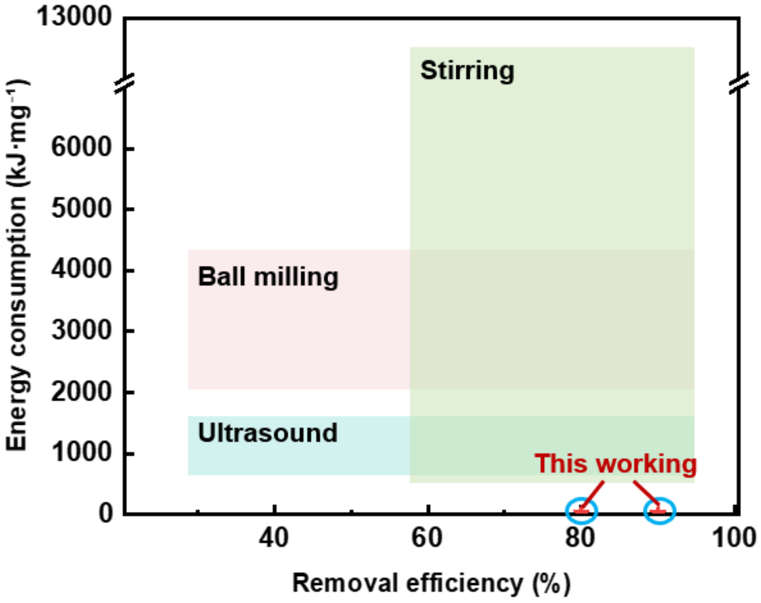

Fig. S14 Comparison of removal efficiency and energy consumption for different activated CEC methods in dye degradation.

References

Cao D Q, Fang R K, Song Y X, Ma M G, Li H, Hao X D, Wu R, Chen X (2024). Contact-electro-catalysis for degradation of trace antibiotics in wastewater. Chemical Engineering Journal, 487

Chen Z, Lu Y, Liu X, Li J, Liu Q (2023). Novel magnetic catalysts for organic pollutant degradation via contact electro-catalysis. Nano Energy: 108

Delley B (1990). An all‐electron numerical method for solving the local density functional for polyatomic molecules. The Journal of chemical physics, 92(1): 508-517

Dolg M, Wedig U, Stoll H, Preuss H (1987). Energy‐adjusted ab initio pseudopotentials for the first row transition elements. The Journal of chemical physics, 86(2): 866-872

Dong X, Wang Z, Berbille A, Zhao X, Tang W, Wang Z L (2022). Investigations on the contact-electro-catalysis under various ultrasonic conditions and using different electrification particles. Nano Energy, 99: 107346

Lai Y, Li K, Lin S, Zhou L, Yu Z, Yuan Y (2025). Contact-electro-catalysis triggers peroxymonosulfate activation for micropollutant degradation. Science China Technological Sciences, 68(7): 1720502

Ma D, Li W, Zhang J, He K, Zhang C, Wang G, Xin X, Liu Q, Cheng F, Lv S (2024). Fluorocarbon polymers mediated contact-electro-catalysis activating peroxymonosulfate for emerging pollutants degradation: The key role of fluorine density in electron transfer. Chemical Engineering Journal, 497: 154996

Peng J, Zhou P, Zhou H, Liu W, Lai B Insights into the Electron-Transfer Mechanism of Permanganate Activation by Graphite for Enhanced Oxidation of Sulfamethoxazole. Environmental Science & Technology, 55(13): 9189-9198

Ruan L, Jia Y, Guan J, Xue B, Huang S, Wang Z, Fu Y, Wu Z (2022). Tribo-electro-catalytic dye degradation driven by mechanical friction using MOF-derived NiCo2O4 double-shelled nanocages. Journal of Cleaner Production, 345: 131060

Tang Q, Meng Y, Xu Y, Zhang H, Du F, Kong L-B, Liu L, Zhang T, Gao J (2023). Tribocatalytic activity on Ba (Ti0. 95Zr0. 05) O3 surfaces: The role of oxygen vacancies and the aging effect. Materials Science and Engineering: B, 297: 116814

Tang Q, Zhu M, Zhang H, Gao J, Kwok K W, Kong L-B, Jia Y, Liu L, Peng B (2022a). Enhanced tribocatalytic degradation of dye pollutants through governing the charge accumulations on the surface of ferroelectric barium zirconium titanate particles. Nano Energy, 100: 107519

Tang Q, Zhu M, Zhang H, Gao J, Kwok K W, Kong L B, Jia Y, Liu L, Peng B (2022b). Enhanced tribocatalytic degradation of dye pollutants through governing the charge accumulations on the surface of ferroelectric barium zirconium titanate particles Nano Energy,

Wang X, Wang Y, Zhao C, Zhu Y, Sun Z, Fan H J S, Hu X, Zheng H (2021). Ciprofloxacin removal by ultrasound-enhanced carbon nanotubes/permanganate process: In situ generation of free reactive manganese species via electron transfer. Water Research, 202: 117393-

Wang Z, Berbille A, Feng Y, Li S, Zhu L, Tang W, Wang Z L (2022). Contact-electro-catalysis for the degradation of organic pollutants using pristine dielectric powders. Nature Communications, 13(1): 130

Wang Z, Dong X, Li X-F, Feng Y, Li S, Tang W, Wang Z L (2024). A contact-electro-catalysis process for producing reactive oxygen species by ball milling of triboelectric materials. Nature Communications, 15(1): 757

Wu M, Xu Y, He Q, Sun P, Weng X, Dong X (2022). Tribocatalysis of homogeneous material with multi-size granular distribution for degradation of organic pollutants. Journal of colloid and interface science, 622: 602-611

Wu Z, Wu S, Zhang L, Wu Z, Hong S, Chen B, Zhu G, Jia Y (2025). Low-frequency contact-electro-catalysis driven by friction between the PTFE-coated fabric and dye solution. Journal of Alloys and Compounds, 1010

Yadav P, Manori S, Shukla R K (2024). Contact electro catalysis driven degradation of malachite green dye by RGO/ZnO nanohybrid. Solid State Communications: 389

Yang T, Mai J, Zhu M, Peng Q, Huang C, Wu S, Tan Q, Jia J, Fang J, Ma J (2022). Enhanced permanganate activation under UVA-LED irradiation: unraveled mechanism involving manganese species and hydroxyl radical. Environmental Science & Technology, 56(24): 17720-17731

Yin F, Liu J H, Zhang Y, Liu M N, Wang L Y, Yu Z C, Yang W H, Zhang J, Long Y Z (2024). Contact‐Electro‐Catalysis for Organic Pollutants Degradation Based on 2D Fluorinated Graphite. Advanced Functional Materials, 34(41)

Yingying X, Rongyang Y, Yaning Z, Baocheng Z, Pengfei S, Xiaoping D (2022). Unveiling the Mechanism of Frictional Catalysis in Water by Bi12TiO20: A Charge Transfer and Contaminant Decomposition Path Study. Langmuir : the ACS journal of surfaces and colloids, 38(46)

Zhang B, Xia S, Wang Z, Li W, Li B, Zhang H, Xin Y, Wu K, Ma J, He X (2024). Enhanced permanganate activation by g-C3N4 under visible light irradiation: Unraveled mechanism involving Mn(V) and photo-induced electron. Applied Catalysis B: Environmental, 349(000)

Zhao X, Su Y, Berbille A, Wang Z L, Tang W (2023). Degradation of methyl orange by dielectric films based on contact-electro-catalysis. Nanoscale, 15(13): 6243-6251